GEOPHYSICS, VOL. 79, NO. 4 (JULY-AUGUST 2014); P. B173–B185, 14 FIGS., 3 TABLES.
10.1190/GEO2014-0029.1

Case History

Cooperative constrained inversion of multiple electromagnetic data sets

Michael S. McMillan[1] and Douglas W. Oldenburg[1]

ABSTRACT

We evaluated a method for cooperatively inverting multiple electromagnetic (EM) data sets with bound constraints to produce a consistent 3D resistivity model with improved resolution. Field data from the Antonio gold deposit in Peru and synthetic data were used to demonstrate this technique. We first separately inverted field airborne time-domain EM (AEM), controlled-source audio-frequency magnetotellurics (CSAMT), and direct current resistivity measurements. Each individual inversion recovered a resistor related to gold-hosted silica alteration within a relatively conductive background. The outline of the resistor in each inversion was in reasonable agreement with the mapped extent of known near-surface silica alteration. Variations between resistor recoveries in each 3D inversion model motivated a subsequent cooperative method, in which AEM data were inverted sequentially with a combined CSAMT and DC data set. This cooperative approach was first applied to a synthetic inversion over an Antonio-like simulated resistivity model, and the inversion result was both qualitatively and quantitatively closer to the true synthetic model compared to individual inversions. Using the same cooperative method, field data were inverted to produce a model that defined the target resistor while agreeing with all data sets. To test the benefit of borehole constraints, synthetic boreholes were added to the inversion as upper and lower bounds at locations of existing boreholes. The ensuing cooperative constrained synthetic inversion model had the closest match to the true simulated resistivity distribution. Bound constraints from field boreholes were then calculated by a regression relationship among the total sulfur content, alteration type, and resistivity measurements from rock samples and incorporated into the inversion. The resulting cooperative constrained field inversion model clearly imaged the resistive silica zone, extended the area of interpreted alteration, and also highlighted conductive zones within the resistive region potentially linked to sulfide and gold mineralization.

INTRODUCTION

Electromagnetics (EM) is an important tool in mineral exploration because it produces 3D computer models of electrical resistivity distributions in the subsurface of the earth. Electrical resistivity, hereafter resistivity, measures the degree to which a material opposes the flow of electric current, and this physical property can help distinguish rock types and alteration zones due to resistivity contrasts compared to background lithologies (Keller, 1988). Resistivity, and its reciprocal, conductivity, will be referred to throughout this paper. Conventionally, an individual EM survey is inverted with finite-volume (Haber et al., 2007a), finite-difference (Commer and Newman, 2004), or integral equation techniques (Cox et al., 2010), to create a single resistivity inversion model. However, when multiple spatially overlapping surveys, possibly from different time periods, produce inconsistent inversion models, this can lead to difficulties in interpretation. These model discrepancies suggest that a joint or cooperative approach, in which one consistent inversion model is sought, could be beneficial.

In a joint inversion, multiple data are inverted simultaneously (Vozoff and Jupp, 1975; Haber and Oldenburg, 1997; Albouy et al., 2001; Gallardo and Meju, 2004; Sosa et al., 2013). This requires

Manuscript received by the Editor 20 January 2014; published online 12 June 2014.
[1]University of British Columbia, Department of Earth, Ocean and Atmospheric Sciences, Geophysical Inversion Facility, Vancouver, British Columbia, Canada. E-mail: mmcmilla@eos.ubc.ca; doug@eos.ubc.ca.

being able to forward model and compute sensitivities for all data within a single code, and it also requires proper relative assignments of uncertainties. Any problematic data within the entire suite of data can cause the inversion to proceed very slowly, and it may produce unwanted artifacts in the final model. In a cooperative inversion, results from inverting one data set are used in the inversion of another data set (Lines et al., 1988; Oldenburg et al., 1997; Commer and Newman, 2009).

There are numerous ways to implement this cooperation through the use of reference models, constraints, or weightings in the regularization term of the objective function. The advantage of a cooperative approach is that individual algorithms, tailored to inverting a particular type of data, can be used. This is beneficial because carrying out inversions of multiple data sets individually is generally much faster than inverting them simultaneously. The potential disadvantage of cooperative inversion is that there are many strategies that could be invoked in an attempt to find a single model that fits both data sets. Therefore, a cooperative inversion needs a set methodology or workflow to address specific issues in implementation. In this paper, we model direct current (DC) resistivity data as a very low frequency domain survey, and hence both DC resistivity and controlled-source audio-frequency magnetotellurics (CSAMT) can be jointly inverted using our generalized frequency domain code. We do, however, adopt a cooperative strategy when airborne time-domain EM (AEM) data are included. We have three primary research objectives in this study:

1) to develop a cooperative inversion method that incorporates multiple spatially overlapping geophysical EM data sets and borehole constraints
2) to prove, with a synthetic example, that a cooperative method increases the accuracy of the resulting 3D resistivity model
3) to apply a cooperative approach to field data to produce a consistent inversion model in which additional geologic interpretations can be established.

We first present three spatially overlapping data sets over the Antonio high-sulfidation epithermal gold deposit: AEM, CSAMT, and DC resistivity. Each survey is inverted individually in 3D to estimate a resistivity structure sensitive to that particular survey. Similarities and differences in the resulting models are noted. The inversion results and available geophysical/geologic insight about the deposit are then used to construct a synthetic model that emulates, as close as possible, the Antonio deposit. Simulated data sets, using field measurement locations, are computed over the synthetic model. Synthetic data are inverted individually to ascertain whether differences again occur between resulting models. At this point, we introduce a cooperative approach, which improves the accuracy of the synthetic inversion model in a qualitative and quantitative sense. This cooperative workflow is then applied to the Antonio field data. As a subsequent step, we carry out a cooperative inversion but apply bound constraints from borehole information. This is first done in the synthetic case to observe if further improvement is made and then to the field data sets. This yields a final model from which geologic interpretations are made.

Figure 1. Map of Peru with location of the Antonio deposit marked as a black star.

GEOLOGIC BACKGROUND

The Antonio gold deposit is located in the Andes mountains of Northern Peru, as shown in Figure 1, and resides within the larger Yanacocha high-sulfidation epithermal gold system. Newmont Mining Corporation owns most of this active mining and exploration project. The region experienced pervasive hydrothermal alteration to form a zone of massive silicic alteration in the innermost zone, flanked by alunite, pyrophyllite, kaolinite, and montmorillonite assemblages with an outermost halo of propylitic alteration (Teal and Benavides, 2010). This alteration zonation is characteristic of high-sulfidation deposits (Arribas, 1995). The bulk of the gold mineralization resides within massive silica, vuggy silica, and granular silica units, and these quartz-rich areas of metasomatism are often found near faults where confined fluid flow occurred (Teal and Benavides, 2010). Furthermore, the intersection of faults, where hydrothermal breccias broke through overlaying volcanic units, is especially prospective for gold mineralization. These structural traps within favorable pyroclastic lithologies, such as ignimbrite beneath or proximal to flow dome complexes, are typical geologic hosts to gold deposits in the region (Loayza and Reyes, 2010). Much of the surrounding clay alteration at Antonio has also been enriched with silica, and for the sake of this study, any zone significantly enriched with quartz is referred to as silica alteration. The resistive nature of silica alteration compared to the relatively conductive background makes it an applicable target for EM and DC surveys (Goldie, 2000; Oldenburg et al., 2005; Hoschke, 2011). Figure 2 shows a geologic map of the Antonio region with common lithologies and

structures marked. The primary extent of near-surface (0–100 m depth) silica alteration is outlined in dashed red.

GEOPHYSICAL SURVEYS

AEM

In 2003, a helicopter-based time-domain AEM survey was collected using the NEWTEM I system (Eaton et al., 2013). Five east–west lines over the Antonio deposit, extracted from the larger airborne survey, are analyzed in this study. The peak current of the transmitter was 245 A, with a transmitter loop area of 289 m^2. Vertical $d\mathbf{B}/dt$ responses, measured out to 6.35 ms after current shut off were recorded every 20 m with a line spacing of 200 m for a total of 268 transmitter positions. Time channels from 30 to 2000 μs are used for analysis. Due to the mountainous terrain, the drape of the transmitter above the ground varied from 32 to 146 m, with a mean value of 62 m. Exact system locations are shown as orange circles in Figure 3.

CSAMT

In 2003, an asynchronous scalar CSAMT (Zonge and Hughes, 1991) survey was acquired by Quantec Geoscience with a total of five east–west and eight north–south lines over the Antonio deposit. Two transmitters: an east–west-oriented transmitter 6.2 km to the south, and a north–south-oriented transmitter 5.9 km to the east provided the source for east–west and north–south lines, respectively. Having transmitters with orthogonal orientations permitted the earth to be energized from two directions. Line spacings varied between 150 and 200 m, and stations were spread 50 m apart. Inline electric-field (E-field) and orthogonal magnetic-field (H-field) measurements from 11 frequencies ranging between 2 and 2048 Hz are used in this study. The receiver locations are shown as red stars in Figure 3.

DC resistivity

In 1998, a conventional in-line time-domain pole-dipole DC resistivity survey was acquired with five east–west lines spread 150–200 m apart with 50 m spaced dipoles, and a transmitter/receiver separation, commonly referred to as n-spacing, of one to six for the variable n. In 2004, one additional line of 150 m spaced dipoles situated 50 m south of the previous survey was collected. Receiver locations are shown as green triangles in Figure 3. Examples of field data from each survey can be seen in Figure 4.

METHODS

Inversion preparation

Prior to inverting field data, initial steps such as quality control of the data, preparing suitable meshes, and assigning appropriate uncertainty values need to be completed, as well as removing field data below an estimated noise threshold. Even though inversions

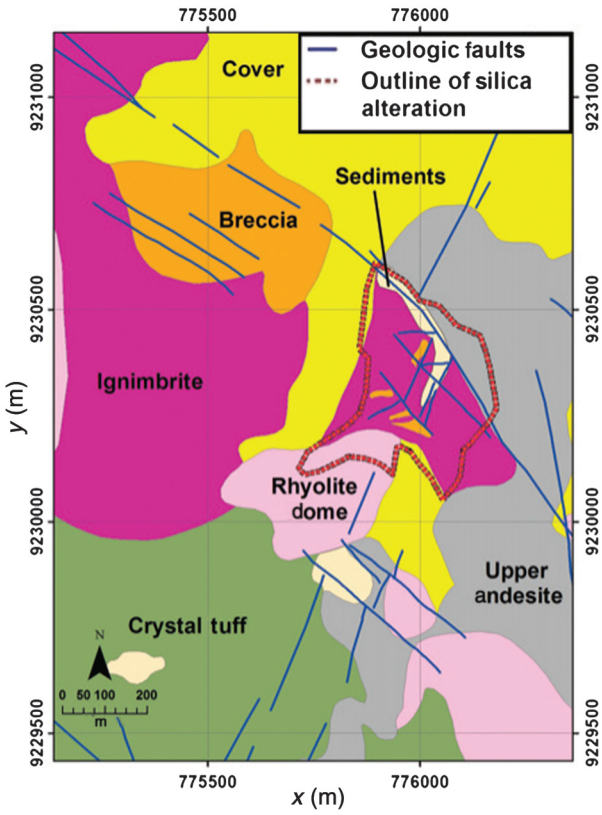

Figure 2. Antonio geology with lithologies, structures, and near-surface silica alteration outlined.

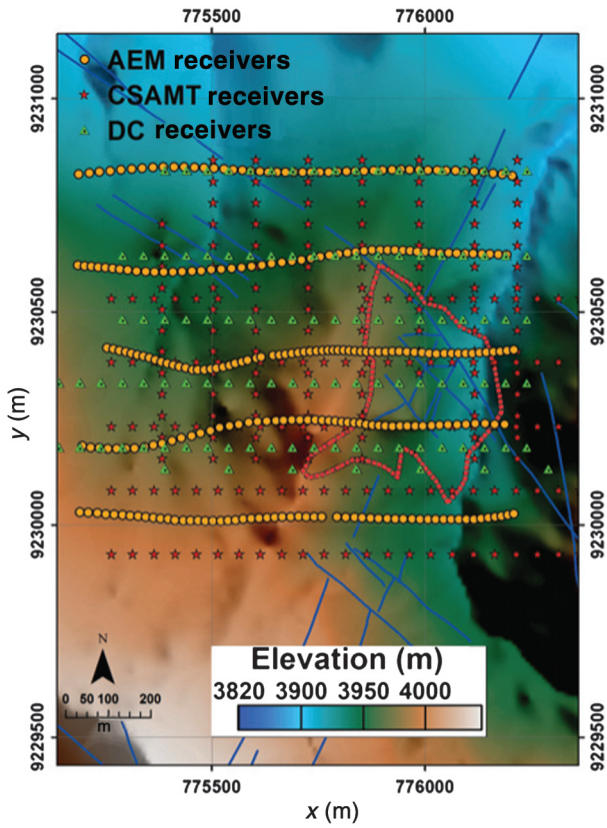

Figure 3. Antonio geophysics locations. Receiver sites for AEM (orange circles), CSAMT (red stars), and DC resistivity (green triangles) overlaid on topography with the near-surface silica alteration outlined in dashed red lines, and the geologic faults are shown in thin blue lines.

are carried out separately in a cooperative inversion, it is desirable to have a common mesh so difficulties in transferring results from different meshes are avoided. Here, because we have frequency- and time-domain surveys, the design of the mesh is based on the diffusion distance and skin depth (Nabighian and Macnae, 1988; Ward and Hohmann, 1988):

$$d = \sqrt{\frac{2t}{\mu_0 \sigma}} \tag{1}$$

$$\delta = \sqrt{\frac{2}{\mu_0 \sigma \omega}} \tag{2}$$

where d and δ are the diffusion distance and skin depth, respectively; t is time; μ_0 is the magnetic permeability of free space; σ is the conductivity; and ω is the angular frequency. To minimize numerical accuracy issues, mesh creation in this study adheres to the guidelines below, which are based on experience working with these codes:

- The mesh contains padding cells extending to a minimum of twice the largest diffusion distance, or twice the largest skin depth. For a 50 Ωm half-space, this equates to roughly 4 km of padding around the core area of interest for AEM and 5 km of padding around the CSAMT receivers.
- The smallest cell size in the mesh is at most half the minimum diffusion distance or minimum skin depth. For a 50 Ωm half-space, this produces a minimum cell size of 24 and 40 m for AEM and CSAMT, respectively.

In an inversion, there is always a trade-off between accuracy and total size of the mesh. Because the highest numerical error is confined to a limited number of time channels and frequencies, we do not believe that numerical accuracy is a concern with the above guidelines. The final mesh, designed to be suitable for all three surveys, contains core cell sizes of $25 \times 50 \times 25$ m in x, y, z around all receiver and transmitter locations. To accommodate CSAMT transmitters far away from the receiver area without greatly increasing the number of total cells, an adaptive octree mesh is used (Haber et al., 2007b). The final number of cells in the overall mesh is 86,942 with a total spatial extent of $12.8 \times 12.8 \times 6.4$ km in x, y, z.

The next task is to assign uncertainties to the data. The assigned error uncertainty is made up of a percentage and a floor value. Percentages range between 10% and 15%, depending on the noisiness of the data. The noise floor was chosen as two standard deviations below the logarithmic mean of the absolute value of the data. This may be somewhat optimistic for the AEM data because the original AEM noise floor of 5 μV had difficulties converging to a solution, so it was later raised to 30 μV.

Inversion methodology

The AEM, CSAMT, and DC inversions follow algorithms outlined in Oldenburg and Li (1994) and Haber et al. (2004, 2007a), which minimize an objective function

$$\phi = \phi_d + \beta \phi_m \tag{3}$$

to obtain an optimal conductivity distribution, where ϕ_d is the data-misfit, ϕ_m is the model regularization term, and β is a trade-off parameter. The data misfit is defined by a least-squares measure

$$\phi_d = \|\mathbf{W}_d(\mathbf{d}^{\text{obs}} - \mathbf{d}^{\text{pred}})\|_2^2, \tag{4}$$

where $\mathbf{d}^{\text{obs}}$ is an observation vector, $\mathbf{d}^{\text{pred}}$ is a predicted data vector, $\mathbf{W_d}$ is a diagonal matrix containing the reciprocal of data error standard deviations, and $\|\|_2^2$ is the squared ℓ^2 norm. The model regularization term is given by

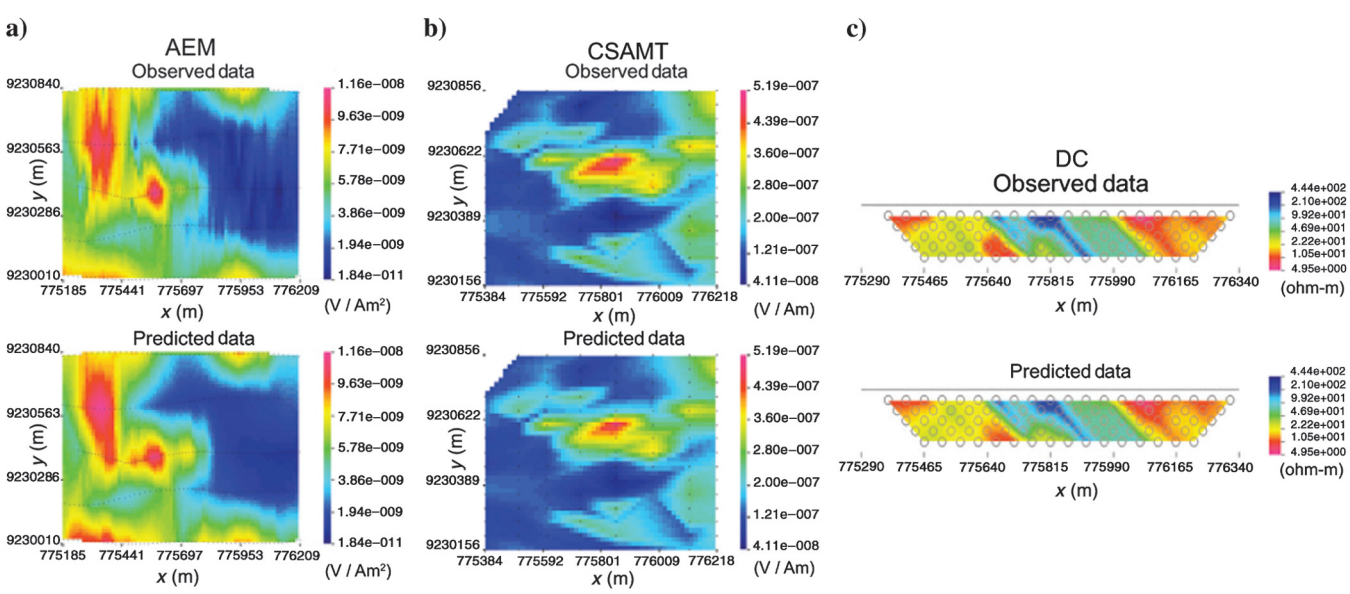

Figure 4. Observed and predicted field data from individual inversions: (a) AEM plan view of the z-component $d\mathbf{B}/dt$ at 139 μs, (b) CSAMT plan view of the y-component electric field at 16 Hz, and (c) DC apparent resistivity pseudosection from line 9230630.

$$\phi_m = \alpha_s \int_{\mathbf{V}} \mathbf{W}_s(\mathbf{m}-\mathbf{m}_0)^2 \mathrm{d}\mathbf{V} + \alpha_x \int_{\mathbf{V}} \mathbf{W}_x \left(\frac{\partial \mathbf{m}}{\partial x}\right)^2 \mathrm{d}\mathbf{V} + \alpha_y \int_{\mathbf{V}} \mathbf{W}_y \left(\frac{\partial \mathbf{m}}{\partial y}\right)^2 \mathrm{d}\mathbf{V} + \alpha_z \int_{\mathbf{V}} \mathbf{W}_z \left(\frac{\partial \mathbf{m}}{\partial z}\right)^2 \mathrm{d}\mathbf{V}, \quad (5)$$

where the α values are user-defined weights, $\mathbf{W}$ terms are diagonal weighting matrices, $\mathbf{m}$ is a model vector, $\mathbf{m}_0$ is a reference model vector, and $\mathbf{V}$ is a volume matrix. The minimization of the objective function at the $(i+1)$th iteration in a Gauss-Newton method requires the solution of

$$(\mathbf{J}^T\mathbf{W}_d^T\mathbf{W}_d\mathbf{J} + \beta\mathbf{R}_m)\delta\mathbf{m} = -\mathbf{J}^T\mathbf{W}_d^T\mathbf{W}_d(\mathbf{d}_{\mathrm{obs}} - \mathbf{d}^{(i)}) - \beta\mathbf{R}_m(\mathbf{m}^{(i)} - \mathbf{m}_0), \quad (6)$$

where $\mathbf{J}$ is a Jacobian matrix of sensitivities, $\mathbf{R}_m$ is a regularization matrix, and $\delta\mathbf{m}$ is a model perturbation vector. For this study, three Gauss-Newton iterations are computed for each β value, which is referred to as one "beta" iteration. The inversion terminates when the data misfit reaches its target level ϕ_d^*, which equals the total number of data points.

FIELD INVERSIONS

The 3D inversions for all individual field data sets are performed, and examples of predicted data results are shown in Figure 4. Resistivity plan maps at a constant elevation of 3870 m above sea level through the resulting models are shown in Figure 5 with a consistent color scale. Due to rolling topography, a constant elevation slice of 3870 m corresponds to an average depth below surface of roughly 75 m, although it ranges from 10 to 150 m throughout the survey area. These inversions are unconstrained and use a 50 Ωm half-space reference model. Details about uncertainty assignments and final data misfits are summarized in Table 1. Geologic faults and the outline of known near-surface silica alteration are plotted for reference. Figure 5a shows a slice through the AEM 3D inversion model along with data locations, and the result recovers a large uniform resistor in the center of the survey area. This anomaly agrees well with the known resistive silica alteration outline, and past studies (Oldenburg et al., 2004, 2005), although the resistor extends past the known outline to the northwest for approximately 200 m.

Figure 5b portrays a 3870 m constant elevation slice through the 3D CSAMT inversion result along with receiver locations. Due to the asynchronous nature of the CSAMT survey, only the amplitude of the electric and magnetic fields are inverted. The imaged resistor has some similarity to that from the AEM inversion, but it deviates more from the known silica alteration outline. Although the recovered resistivity magnitudes compare well with that from AEM, the center of the CSAMT anomaly is shifted to the west, and the resistor extends 100 to 200 m west of the mapped alteration zone. The CSAMT anomaly is broken up into multiple pieces, unlike the cohesive AEM image, and some small conductive areas occur within the resistive region. There is also a spurious anomaly in the extreme northwest corner of Figure 5b, which is outside the data-supported region and should be ignored.

The inversion of DC potential differences is shown as a 3870 m constant elevation slice in Figure 5c, along with receiver electrode

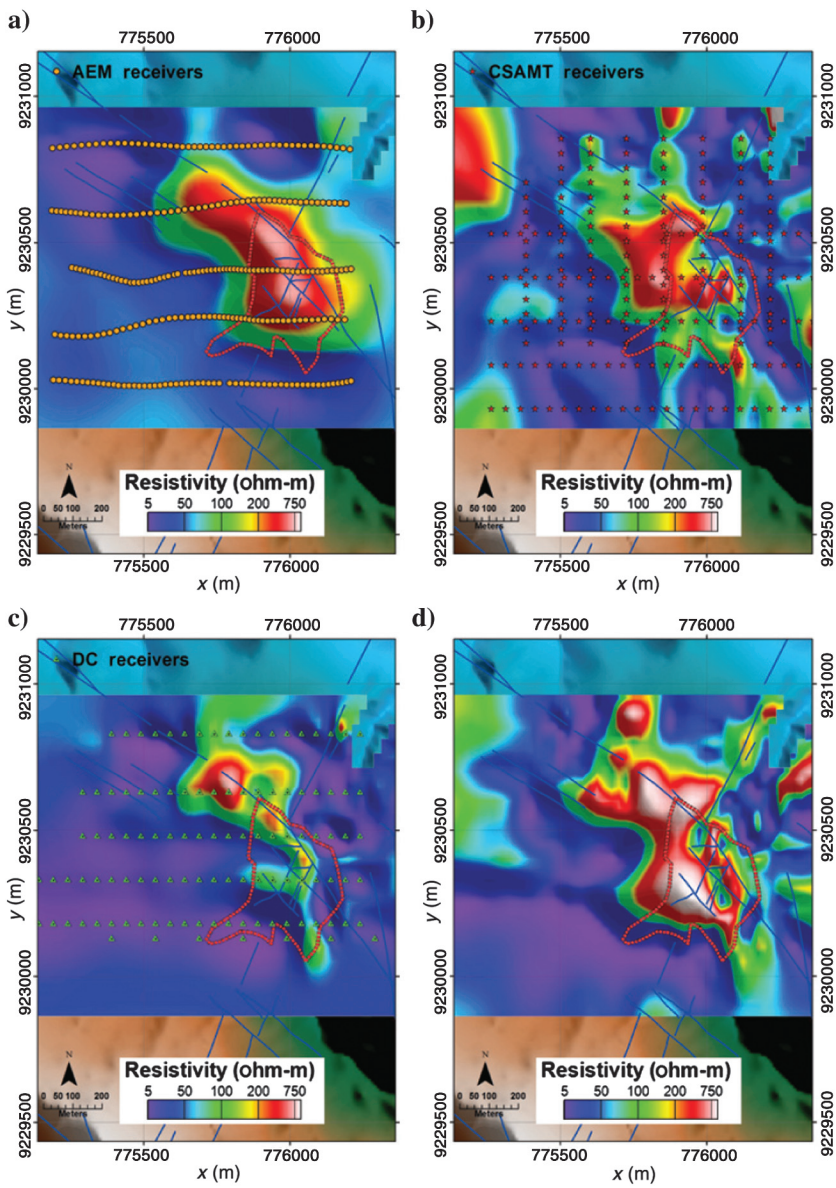

Figure 5. Resistivity 3D inversions from field data at a 3870 m elevation slice with receiver locations shown. The near-surface silica alteration outline is shown in dashed red lines, and the geologic faults appear in thin solid blue lines: (a) AEM, (b) CSAMT, (c) DC resistivity, and (d) cooperative.

Table 1. Error assignments and final data misfits for individual field and synthetic inversions.

Data set	Error (%)	Error (floor)	Target ϕ_d^*	Final ϕ_d
Field				
AEM	15	30 μV	3752	3673
CSAMT	10	3.5×10^{-8} V/m (E-field)	2849	2722
		2.7×10^{-8} A/m (H-field)		
DC	10	0.5 mV	570	519
Synthetic				
AEM	10	30 μV	3752	3747
CSAMT	10	1.0×10^{-9} V/m (E-field)	5698	2982
		1.0×10^{-9} A/m (H-field)		
DC	10	1.5 mV	570	408

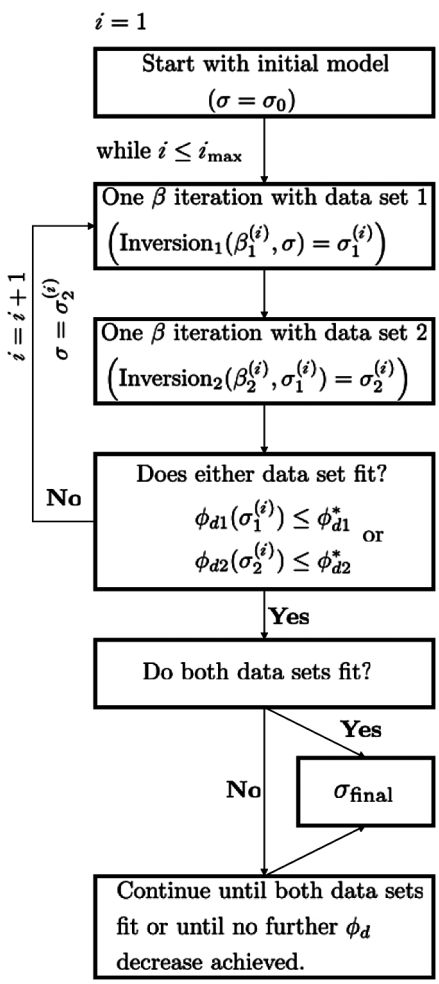

Figure 6. Cooperative inversion workflow. $\sigma_j^{(i)}$ = conductivity model from the ith β iteration for data set j, β = trade-off parameter, ϕ_d = data misfit, and ϕ_d^* = target data misfit.

locations. The recovered model exhibits a similar curved north-northwest-trending resistivity feature as the AEM survey, although the strongest resistor occurs outside the dashed outline to the northwest. Within the known alteration zone, much of the area is modeled as conductive, although there is a thin resistive feature that extends down through the marked anomaly to the southeast portion of the survey. Resistivity magnitudes are generally weaker compared to AEM and CSAMT results, and the overall shape is narrower and smaller compared to the other two models.

COOPERATIVE INVERSION

Discrepancies between individual field inversion results suggest that joint and/or cooperative methods are warranted to produce one resistivity model that fits all the data sets. Intrinsically, this may be challenging. The different surveys can have their own problems, and each source can interact differently with the earth. Complications due to anisotropy, data quality variations, acquisition location differences, modeling errors, and different source types (galvanic versus inductive) can complicate results. Here, we have no reason to believe that anisotropy is a major factor; therefore, we assume that the resistivity is isotropic, and we generate a numerical modeling mesh that is satisfactory for all data sets. We invert the AEM data cooperatively with a joint CSAMT/DC data set. In our joint CSAMT/DC data set, DC voltages are first converted into electric fields and then treated as a 0.125 Hz frequency input in the CSAMT data. This frequency is sufficiently low such that there are no inductive effects observed in the simulated data.

Our cooperative workflow is proposed in Figure 6. Starting with an initial model σ_0, the first task is to take a single Gauss-Newton step for inverting data d_1 with a starting beta $\beta_1^{(1)}$, where the subscript refers to data set (d_1), and the superscript in parentheses refers to the β iteration. This first Gauss-Newton step produces an updated model $\sigma_1^{(1)}$. This updated model becomes the initial and reference model for the first β iteration for data set d_2, and the output is $\sigma_2^{(1)}$. Subsequently, this becomes the initial and reference model for a second β iteration. The values of β for this next, and future, iterations are reduced according to a schedule $\beta_1^{(i+1)} = \gamma\beta_1^{(i)}$ and $\beta_2^{(i+1)} = \gamma\beta_2^{(i)}$, where $\gamma \leq 1$. For the work here, we have chosen $\gamma = 0.2$.

This cooperative workflow continues, up to a maximum number of iterations $i_{\max}$, until the target misfit is reached for one or both data sets. If a single model hits both target misfits, ϕ_{d1}^* for d_1 and ϕ_{d2}^* for d_2, each data set has been adequately fit and the process stops.

If only one data set is fit, i.e., d_1, then the emphasis shifts to continued β iterations for d_2. It the output model $\sigma_2^{(i)}$ is still compatible with the d_1 data set, then further β iterations are performed on d_2. If the misfit for d_1 is significantly increased, then a β iteration on d_1 is performed by starting with the last used β_1^i and the cooperative inversion cycle resumes. At this point, if the misfit for d_2 increases, we feel that we have done as well as possible and the current model is accepted as the final result. The strategy is automated and requires only a few user parameters.

SYNTHETIC INVERSION MODELING

Individual synthetic inversions

In synthetic modeling, we simulate data over a predefined resistivity distribution and then attempt to recover the original model by inverting the data. Our synthetic model is designed to encapsulate the primary features of the Antonio area. It includes a 225-m-thick 1000 Ωm resistor placed in a uniform 50 Ωm background. Two conductive 10 Ωm blocks with dimensions of $100 \times 150 \times 100$ m are embedded. The northern conductive block is buried 75 m below the surface, whereas the southern block is exposed at the surface. Topography for the Antonio area is used for the synthetic study. Figure 7 shows a 3870 m constant elevation slice through this synthetic model.

Forward modeling of AEM, CSAMT, and DC surveys is carried out by keeping data locations and other specifications equivalent to those of the field setups. Ten percent Gaussian noise is added to the measurements prior to inversion. Error assignments and final data misfit values are summarized in Table 1. Constant elevation slices at 3870 m through the resulting inversions are shown in Figure 8. The images all display a resistive body centered in the correct location, but the extent of the resistor and the ability to detect the conductive blocks vary between the three models. In Figure 8a, the AEM inversion is able to image the outline of the resistor but is not able to detect either of the two conductive bodies. Figure 8b shows the CSAMT inversion recovery. The result accurately images the overall resistor geometry, while clearly detecting the southern conductor and faintly identifying the northern anomaly. For CSAMT data, real and imaginary electric and magnetic fields are inverted instead of amplitude-only data as in the field example, and this produces twice the number of data points. Our experience shows that using field components (real and imaginary) can sometimes be marginally better at recovering the true resistivity structure compared to amplitude only, but the differences are not major. However, field components represent a more typical data set collected by industry, and we decided to showcase these to determine a maximum improvement that could be obtained with our cooperative inversion. Error floors for synthetic CSAMT data are also set considerably lower to prevent dramatic underfitting of the data. The DC inversion result is displayed in Figure 8c, which depicts the overall geometry of the resistor and the southern conductive block. Resistivity magnitudes are closer to those in the synthetic model compared to the CSAMT and AEM results; however, the northern block is not seen. So, the three inversions have each produced valuable information but significant differences exist in the models. We now use these data sets to test our workflow for carrying out a cooperative inversion.

Synthetic cooperative inversion

The cooperative workflow from Figure 6 is applied to the synthetic data sets. A common mesh is used for all inversions, and previous error assignments are kept from the individual synthetic inversions with the addition of an error floor of 3.0×10^{-5} V/m for electric fields at 0.125 Hz converted from DC voltages. A convergence curve documenting the data misfit progression for each data set is plotted in Figure 9 and summarized in Table 2. For each beta iteration, there are a maximum of four data misfit evaluations, representing the initial data misfit and the resulting misfit after each Gauss-Newton step. Figure 9a shows that the joint CSAMT/DC data, pictured as plus symbols, hits the target misfit, shown by a dashed line, on the third beta iteration. On the fourth beta iteration, the initial data misfit for the joint data set is still below the target level, and thus no additional model update is performed. Eventually, the process is stopped after iteration seven because the AEM data misfit increases compared to that in iteration six, indicating the inversion is trending in the wrong direction. Therefore, the model after iteration six of the AEM inversion is chosen as the final result. At that point, the CSAMT/DC and AEM final data misfits are very close to their desired target misfits. Figure 8d shows a 3870 m constant elevation slice through this sequential synthetic inversion model. The resistor magnitude and shape are defined more uniformly compared to the individual inversions, and the northern conductor is now better detected. The southern conductor is still clearly defined, although not as strongly as in the individual CSAMT or DC inversion. Although the AEM individual inversion does little to resolve the two conductive targets, it contributes to the cooperative inversion by helping to define the main resistive target. Because AEM is an induction method, it should be sensitive to conductive targets; however, the northern conductor is buried, which masks the signal. Furthermore, the flight lines do not directly pass over the southern conductor. In a resistive setting, the signal level is also smaller, and the conductive responses may be washed out by the Gaussian noise added and by the relatively high uncertainty assignments.

Visual interrogation of the models shows that the cooperative result is better than any of the individual inversions. In an attempt to quantify this numerically, we extract a region of the model that consists of the resistor and its included conductive blocks. We numerically evaluate how close the recovered models are to the true

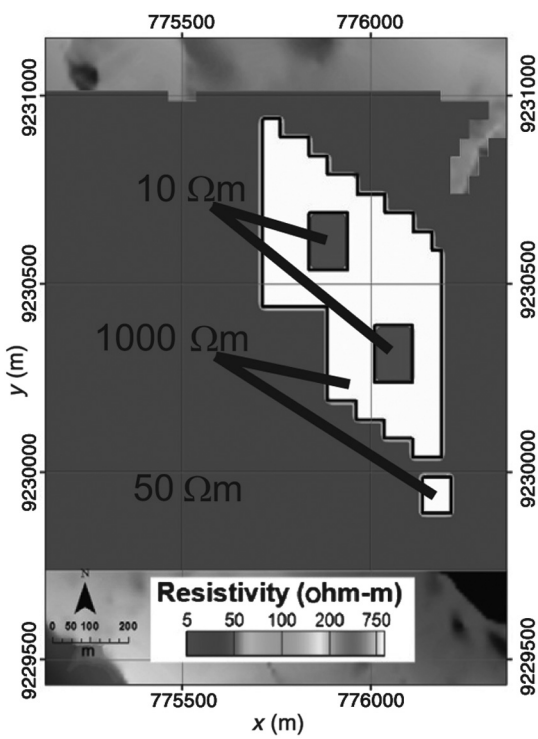

Figure 7. Synthetic model resistivity at a 3870 m elevation slice.

model and consolidate the analysis using the residual (R) as the metric:

$$\mathrm{R} = \frac{1}{N}\|\log_{10}(\mathbf{m}) - \log_{10}(\mathbf{m}_{\mathrm{true}})\|_2^2, \tag{7}$$

where $\mathbf{m}$ and $\mathbf{m}_{\mathrm{true}}$ are the recovered and true resistivity model vectors, respectively, and N is the number of cells in the volume of interest. A lower value of R refers to a smaller deviation from the true model and hence a more accurate recovery. The residuals corresponding to the different inversions, and also the residual that results from a 50 Ωm half-space that is used as a starting model in the inversions, are shown in Table 3. The cooperative inversion performs the best, followed closely by the DC result, whereas the CSAMT and AEM models fare increasingly worse. As expected, all four inversions recover a more accurate model compared to a uniform 50 Ωm half-space. This synthetic example demonstrates that a cooperative method improves the accuracy of the recovered anomalies. Because of its close association with the field data example, we anticipate that the same conclusion can be applied there.

Field cooperative inversion

We implement our cooperative approach on field data, once again using the same common mesh and error assignments as before. A noise floor of 1.0×10^{-5} V/m is placed on 0.125 Hz electric fields converted from DC data. The convergence curves are plotted in Figure 9b, and the final data misfit values are described in Table 2. The joint CSAMT/DC data set reaches its target level after beta iteration eight, and the inversion terminates after iteration nine, when the AEM data misfit is greater than after iteration eight. The model after the eighth AEM beta iteration is chosen as the end result. The final AEM data misfit of 6063 is well above the target of 3752, which demonstrates that the inversion has a more difficult time fitting AEM measurements to the assigned error levels, compared to CSAMT/DC data, in which the final data misfit is only slightly higher than the target value. A constant 3870 m elevation image of the result is displayed in Figure 5d. The recovered resistive anomaly has better agreement with the silica alteration outline compared to the individual inversions, and additional conductive features are clearly visible within the deposit region. Comparable to the synthetic case, the AEM contributes most to the cooperative result by mapping the extent of the large resistor, whereas the conductive features are largely due to the CSAMT/DC data. The magnitude of the cooperative resistor is slightly stronger than the individual inversions, and the resistive anomaly extends past the mapped outline to the northwest. Erroneous resistive anomalies in the extreme northwest and northeast corner are beyond the data-supported region and should be neglected. As would be expected, the cooperative model is similar to all three individual images in some aspects but not identical to any, and it is interpreted to be a more accurate representation of the resistivity signature over the Antonio deposit.

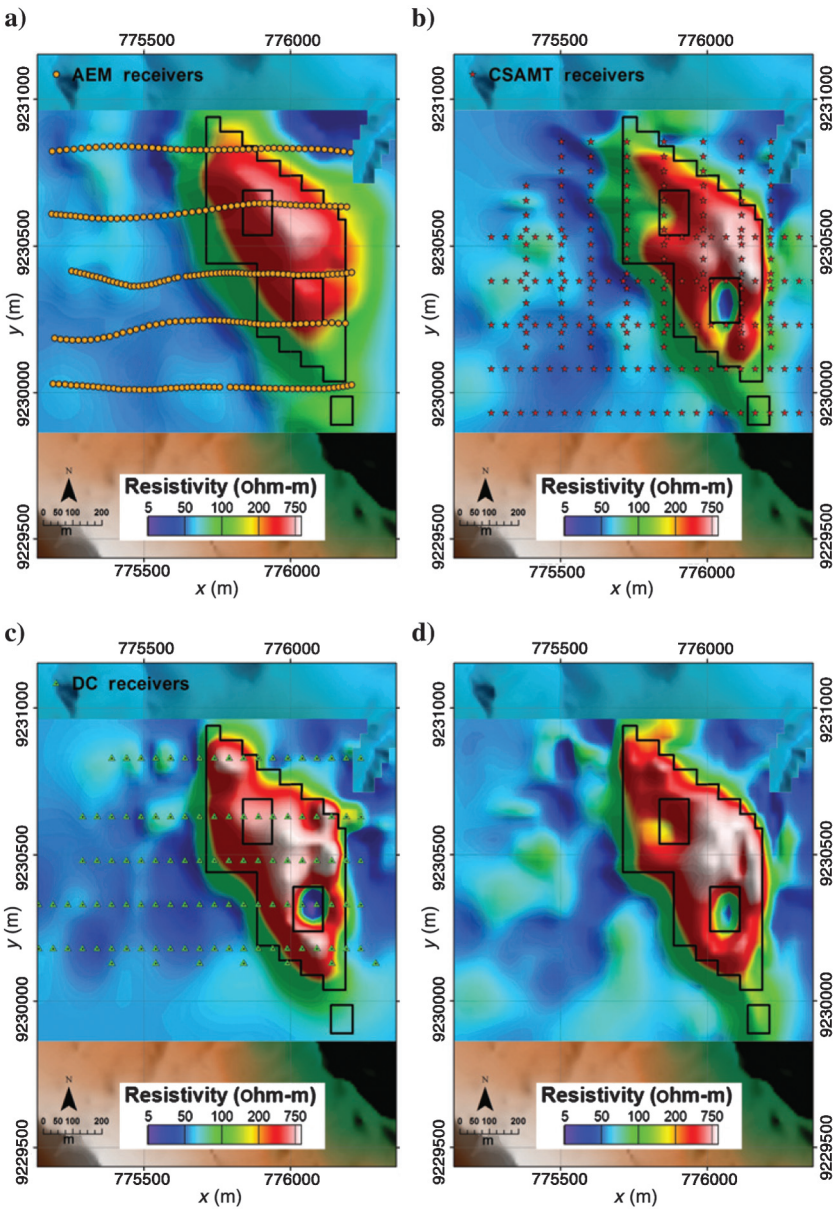

Figure 8. Resistivity 3D inversions from synthetic data at a 3870 m elevation slice with receiver locations shown. The true resistor outline is shown in black: (a) AEM, (b) CSAMT, (c) DC resistivity, and (d) cooperative.

Synthetic constrained cooperative inversion

Thus far, all inversions have been unconstrained, and all start with a 50 Ωm half-space initial and reference model. To test a constrained approach, we refer back to the synthetic example. Constraints are extracted from drilling information from 78 synthetic boreholes, which are replicas of the field boreholes over the Antonio deposit. Each hole intersects multiple discretized cells in the synthetic 3D model, and this

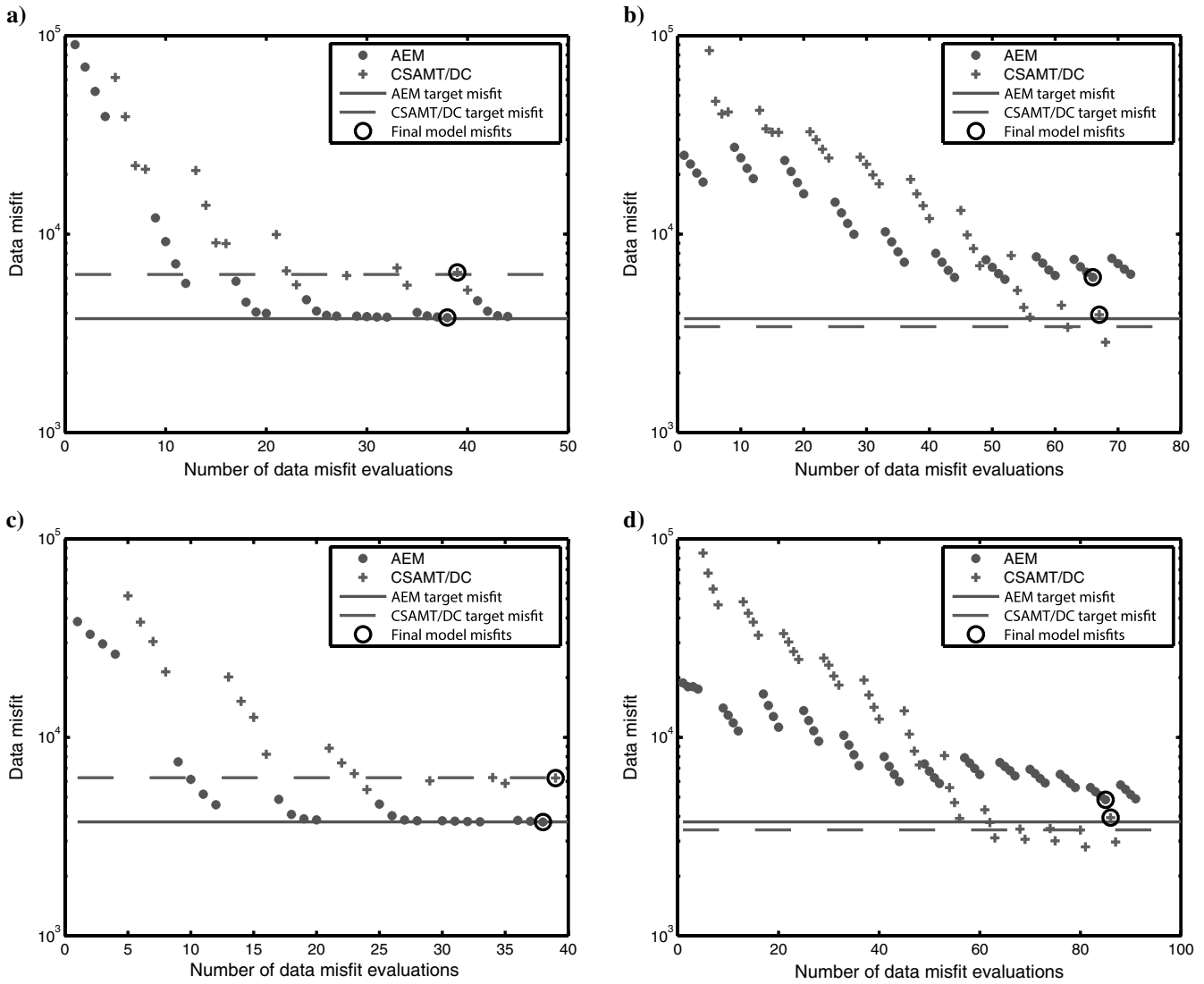

Figure 9. Data misfit convergence curves: (a) synthetic data without bounds, (b) field data without bounds, (c) synthetic data with bounds, and (d) field data with bounds.

Table 2. Final data misfits for cooperative synthetic and field inversions.

Inversion method	Data set	Target ϕ_d^*	Final ϕ_d
Synthetic cooperative	AEM	3752	3798
	CSAMT/DC	6268	6415
Field cooperative	AEM	3752	6063
	CSAMT/DC	3419	3928
Synthetic constrained cooperative	AEM	3752	3745
	CSAMT/DC	6268	6243
Field constrained cooperative	AEM	3752	4853
	CSAMT/DC	3419	3928

Table 3. Quantitative assessment of synthetic inversions using a residual (R) value. A lower residual refers to a more accurate recovery.

Inversion model	Residual (R)
50 Ωm half-space	1.62
AEM	0.80
CSAMT	0.66
DC	0.55
Cooperative	0.47
Bounded cooperative	0.26

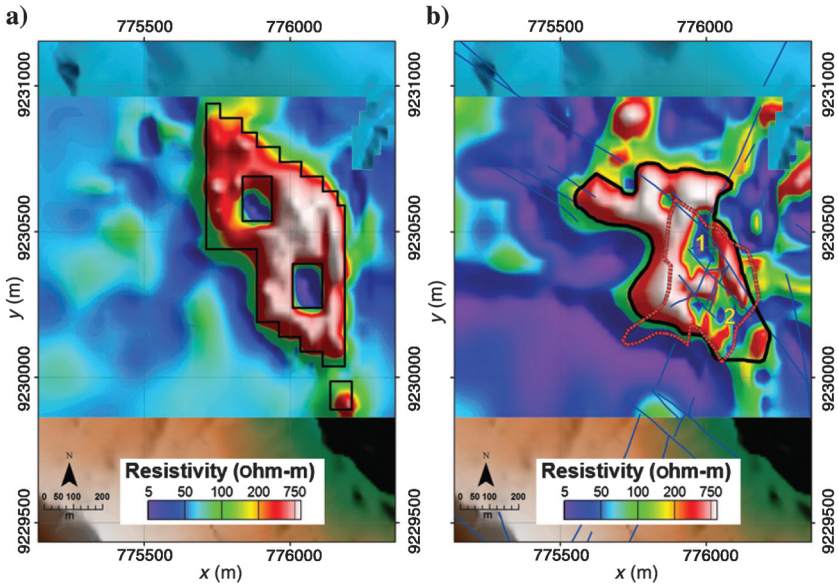

Figure 10. Cooperative 3D inversions with bounds at a 3870 m elevation slice: (a) synthetic data with the true resistor outline in thin black and (b) field data with the outline of known near-surface silica alteration in dashed red, interpreted silica alteration outline at 3870 m elevation in solid black, geologic faults in thin blue, and conductive anomalies of interest numbered in yellow.

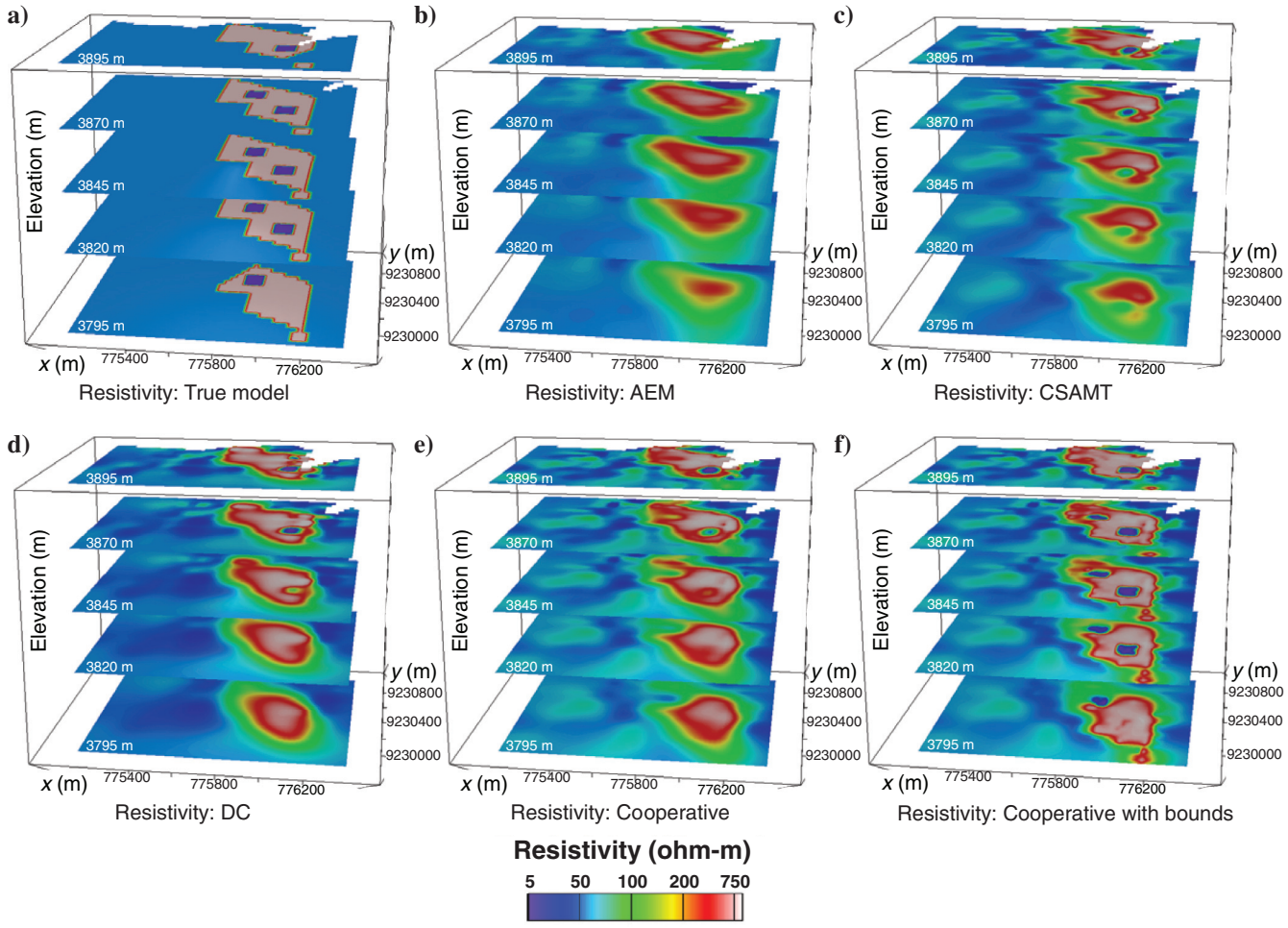

Figure 11. Resistivity 3D inversions from synthetic data at five elevation slices, 3895, 3870, 3845, 3820, and 3795 m: (a) true model, (b) AEM, (c) CSAMT, (d) DC resistivity, (e) cooperative, and (f) cooperative with drilling bounds.

information is used to produce upper and lower resistivity bounds. The upper and lower bounds for each model cell intersected by a borehole are, respectively, set to 5% above and below the corresponding resistivity value in the synthetic model. The regularization of the inversion algorithm attempts to smooth this information away from constrained cells, and a global bound range of 1 to 5000 Ωm is applied to all cells not intersected by boreholes. This global bound prevents extreme inversion artifacts from emerging, and it allows the conductivity to vary freely within this range.

We implement the cooperative method from Figure 6. The convergence plot from Figure 9c shows that after the third beta iteration, the CSAMT/DC data set reaches its target value, and after the sixth AEM β iteration, both data sets reach convergence. Therefore, the addition of bounds helps guide the cooperative approach to a single solution that fits both data sets. A 3870 m constant elevation image of the constrained inversion result is shown in Figure 10a. The outline of the resistor is much improved compared to previous results, and the northern and southern conductors are clearly imaged. Even the small resistive zone at the southern tip of the survey is recovered, thanks primarily to a synthetic borehole. Quantitatively, the constrained cooperative method produces a residual value of 0.26, which outperforms all other synthetic inversions. As a visual summary, constant elevation slices from 3895, 3870, 3845, 3820, and 3795 m are shown in Figure 11 for all synthetic inversions.

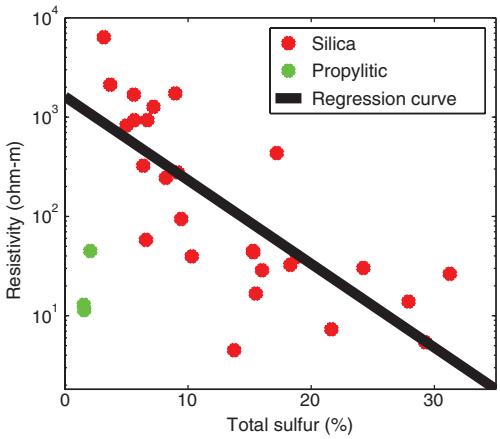

Figure 12. Linear regression curve, shown as a black line, for the resistivity versus total sulfur relationship from 30 borehole samples.

Field constrained cooperative inversion

The constrained cooperative method is now applied to field data, which requires borehole resistivity information. However, boreholes at Antonio have alteration logging and geochemical assay values but only a limited number of resistivity measurements. Surprisingly, from the samples available, there is a poor correlation between alteration or rock type with resistivity; thus, another proxy for resistivity information is needed. Nelson and Van Voorhis (1983) note an inverse relationship between total weight percent sulfide and resistivity for in situ rock measurements in a porphyry environment. Although Antonio is a high-sulfidation deposit and not a porphyry, we investigate this concept by plotting in Figure 12 the total weight percent of sulfur against resistivity for 30 rock samples at Antonio, colored by alteration type. The linear regression curve, represented by the black line in Figure 12, does not include propylitic samples and has a resulting Pearson correlation coefficient of −0.73, indicating a statistical negative correlation. Nearly an identical relationship is extracted when resistivity is compared to total weight percent sulfide, but we focus on total sulfur content because more of these measurements are available.

This regression relationship is applied to the alteration values from 78 field boreholes, whose locations are shown in Figure 13a, and total sulfur content from 61 boreholes, displayed in Figure 13b. The product of the relationship is a resistivity reference model, shown in Figure 13c. Propylitic samples are assigned a resistivity value of 23 Ωm in the reference model, equal to the mean of the three samples in Figure 13a. To create upper and lower bounds, the mean and standard deviation of the resistivity values within each model cell are calculated, and the bounds are set, respectively, to one standard deviation above or below the mean cell value. The

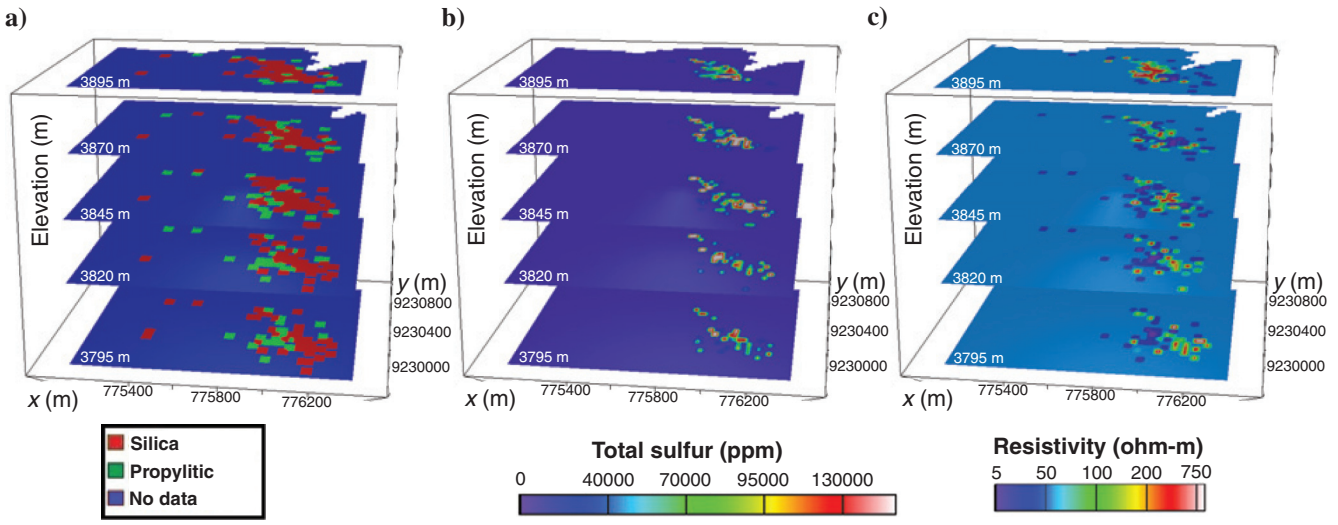

Figure 13. Drilling information for model cells intersected by 78 boreholes at Antonio: (a) alteration, (b) total sulfur content, and (c) resistivity derived from a regression relationship between total sulfur/alteration and resistivity.

incorporation of these bounds to a cooperative constrained field inversion produces the convergence curve shown in Figure 9d. The final target AEM misfit of 4853 is much lower than the unconstrained cooperative inversion, but it is still above the target level, whereas the joint CSAMT/DC final misfit of 3928 is identical to the unconstrained case. A 3870 m constant elevation slice from this model is displayed in Figure 10b. This result has a strong agreement with the known silica outline and with previous studies (Oldenburg et al., 2004, 2005), although some additional features are present, and will be discussed further in the geologic interpretation section.

Caution must be placed when implementing constraints such as upper and lower resistivity bounds because they could erroneously bias the inversion model. Field constraints are derived from a relationship between total sulfur content and resistivity based on 30 laboratory rock measurements. This represents a small sample size from which to produce constraints for an entire model. But the validity of this relationship is corroborated by the similarity between the unconstrained and constrained cooperative inversions. For additional confidence in the bounds, more petrophysical measurements should be acquired, and this is recommended for future constrained cooperative studies.

Geologic interpretation

The constrained cooperative inversion result shown in Figure 10b is considered the final field inversion. This result compares well with the unconstrained cooperative model in Figure 5d, which adds more confidence to the regression relationship that helped calculate the upper and lower resistivity bounds. At an elevation of 3870 m, the resistive zone extends past the mapped alteration outline to the northwest, which suggests that the silica alteration does so as well. Consequently, an outline shown in solid black in Figure 10b represents the interpreted silica alteration zone at 3870 m elevation based on the final field inversion. For completeness, constant elevation slices at 3895, 3870, 3845, 3820, and 3795 m are shown in Figure 14 for all field inversions. In each elevation slice, the final model maps the target silica alteration zone as a strong resistor.

Within the resistive alteration zone from Figure 10b, small conductivity areas are recovered, and two such anomalies are numbered one and two. From borehole alteration logs, anomaly one represents a small area of propylitic alteration, and anomaly two coincides with a large total sulfur anomaly within silica alteration, which suggests extensive sulfide mineralization. This location of inferred

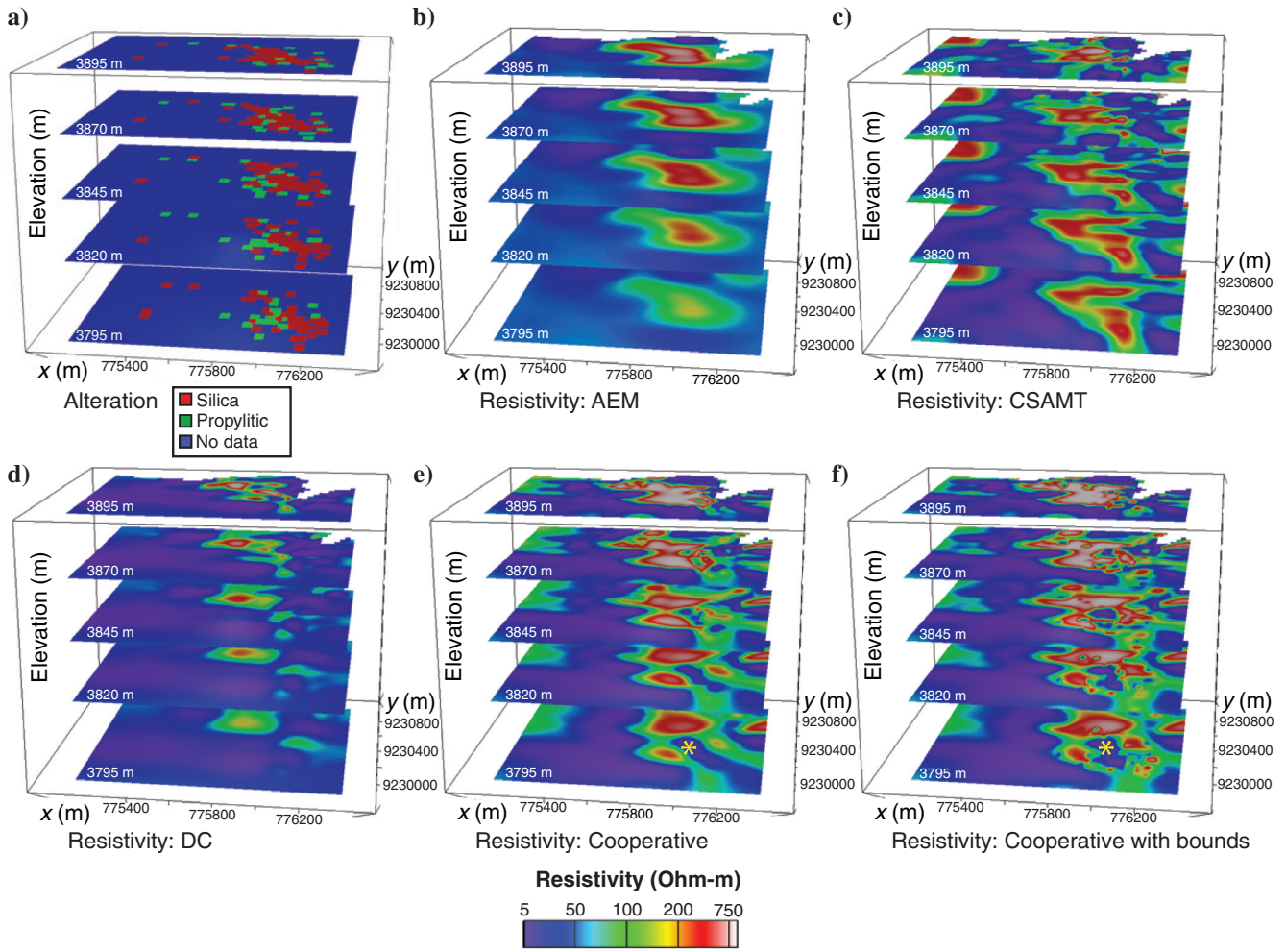

Figure 14. Resistivity 3D inversions from field data at five elevation slices, 3895, 3870, 3845, 3820, and 3795 m: (a) alteration from boreholes, (b) AEM, (c) CSAMT, (d) DC resistivity, and (e) cooperative. An example of a conductive anomaly potentially linked to propylitic alteration is highlighted with a yellow star. Panel (f) shows cooperative with drilling bounds.

sulfide mineralization is potentially explained by its proximity to fault intersections directly to the north and west, where fluid flow would have been confined. Anomaly two also sits on a chargeability high from induced-polarization data. Based on these characteristics, anomaly two is a prime target for gold mineralization. Borehole assays corroborate this observation with anomalous gold values present within anomaly two but not in anomaly one.

At greater depths, many conductive anomalies within the confines of silica alteration can be explained by the presence of propylitic alteration. This agreement is noted even in the unconstrained cooperative inversion in which borehole constraints have not been applied. An excellent example is the large conductive zone at an elevation of 3795 m as shown by yellow stars in Figure 14e and 14f. When compared to the region of propylitic alteration in Figure 14a, there is a strong spatial correlation. Other smaller conductive anomalies within the silica-rich zone not linked to propylitic alteration may indicate the presence of sulfides, and these regions are considered prospective targets for gold mineralization.

CONCLUSIONS

The mineralization at Antonio is known to occur within areas of silica alteration, which is a resistive geophysical target. However, three individual geophysics surveys over the Antonio deposit image the resistivity signature differently. The cooperative inversion method inputs all this information into one physical property model and images the resistive zone at Antonio with a high level of agreement to the known silica alteration. This method is successful in ensuring a consistent inversion result, as demonstrated with a synthetic and field example.

Through synthetic modeling, the cooperative method is shown to improve the accuracy of 3D resistivity inversions. Moreover, adding geologic constraints to the inversion, in the form of upper and lower resistivity bounds for each 3D model cell, produces a result closer to the true synthetic model. Consequently, in a field setting, when reliable borehole physical property information exists, it should be incorporated into the 3D inversion. The final constrained cooperative field model clearly images the large silica alteration zone, and its shape is in general correspondent with drilling and previous studies of the area. An area of silica alteration from the field inversion that extends beyond the previous known outline offers a new interpretation of the mapped alteration. Further analysis from this final model highlights potential areas of sulfide and gold mineralization within the silica alteration zone in the form of small conductive anomalies.

Collectively, this study illustrates that a practical cooperative constrained inversion methodology is possible and that exploration companies could benefit from such a technique for spatially overlapping EM data sets with or without borehole constraints.

ACKNOWLEDGMENTS

The authors thank the Newmont Mining Corporation for permission to show and use the Antonio data. Further thanks go to all the members of UBC-GIF for their help during this research and to the Natural Sciences and Engineering Research Council of Canada (NSERC) for their financial support.

REFERENCES

Albouy, Y., P. Andrieux, G. Rakotondrasoa, M. Ritz, M. Descloitres, J.-L. Join, and E. Rasolomanana, 2001, Mapping coastal aquifers by joint inversion of DC and TEM soundings-three case histories: Groundwater, **39**, 87–97, doi: 10.1111/j.1745-6584.2001.tb00354.x.

Arribas, A., 1995, Characteristics of high-sulfidation epithermal deposits, and their relation to magmatic fluid, *in* J. F. H. Thompson, ed., Magmas, fluids, and ore depositsMineralogical Association of Canada, Short Course Series, vol. 23, 419–454.

Commer, M., and G. A. Newman, 2004, A parallel finite-difference approach for 3D transient electromagnetic modeling with galvanic sources: Geophysics, **69**, 1192–1202, doi: 10.1190/1.1801936.

Commer, M., and G. A. Newman, 2009, Three-dimensional controlled-source electromagnetic and magnetotelluric joint inversion: Geophysical Journal International, **178**, 1305–1316, doi: 10.1111/j.1365-246X.2009.04216.x.

Cox, L. H., G. A. Wilson, and M. S. Zhdanov, 2010, 3D inversion of airborne electromagnetic data using a moving footprint: Exploration Geophysics, **41**, 250–259, doi: 10.1071/EG10003.

Eaton, P. A., R. G. Anderson, S. V. Queen, B. Y. Nilsson, E. Lauritsen, C. T. Barnett, M. Olm, and S. Mitchell, 2013, Helicopter time-domain electromagnetics — Newmont and the NEWTEM experience: Geophysics, **78**, no. 6, W45–W56, doi: 10.1190/geo2012-0472.1.

Gallardo, L. A., and M. A. Meju, 2004, Joint two-dimensional DC resistivity and seismic travel time inversion with cross-gradients constraints: Journal of Geophysical Research, **109**, B03311, doi: 10.1029/2003JB002716.

Goldie, M. K., 2000, A geophysical case history of the Yanacocha gold district, northern Peru: 70th Annual International Meeting, SEG, Expanded Abstracts, 750–753.

Haber, E., U. M. Ascher, and D. W. Oldenburg, 2004, Inversion of 3D electromagnetic data in frequency and time domain using an inexact all-at-once approach: Geophysics, **69**, 1216–1228, doi: 10.1190/1.1801938.

Haber, E., D. W. Oldenburg, and R. Shekhtman, 2007a, Inversion of time domain three-dimensional electromagnetic data: Geophysical Journal International, **171**, 550–564, doi: 10.1111/j.1365-246X.2007.03365.x.

Haber, E., and D. W. Oldenburg, 1997, Joint inversion: A structural approach: Inverse Problems, **13**, 63–77, doi: 10.1088/0266-5611/13/1/006.

Haber, E., S. Heldmann, and U. Ascher, 2007b, Adaptive finite volume method for distributed non-smooth parameter identification: Inverse Problems, **23**, 1659–1676, doi: 10.1088/0266-5611/23/4/017.

Hoschke, T., 2011, Geophysical signatures of copper-gold porphyry and epithermal gold deposits, and implications for exploration: Ph.D. thesis, University of Tasmania.

Keller, G. V., 1988, Rock and mineral properties, *in* M. N. Nabighian, ed., Electromagnetic methods in applied geophysics: vol. 1, SEG 13–52.

Lines, L. R., A. K. Schultz, and S. Treitel, 1988, Cooperative inversion of geophysical data: Geophysics, **53**, 8–20, doi: 10.1190/1.1442403.

Loayza, C., and J. Reyes, 2010, Geologic overview of the Yanacocha mining district: Presented at SIMEXMIN10 — IV Brazilian Symposium of Mineral Exploration.

Nabighian, M. N., and J. C. Macnae, 1988, Time domain electromagnetic prospecting methods, *in* M. N. Nabighian, ed., Electromagnetic methods in applied geophysics: vol. 2, SEG, 427–520.

Nelson, P. H., and G. D. Van Voorhis, 1983, Estimation of sulfide content from induced polarization data: Geophysics, **48**, 62–75, doi: 10.1190/1.1441408.

Oldenburg, D. W., R. A. Eso, S. Napier, and E. Haber, 2005, Controlled source electromagnetic inversion for resource exploration: First Break, **23**, 67–73.

Oldenburg, D. W., and Y. Li, 1994, Inversion of induced-polarization data: Geophysics, **59**, 1327–1341, doi: 10.1190/1.1443692.

Oldenburg, D. W., Y. Li, and R. G. Ellis, 1997, Inversion of geophysical data over a copper gold porphyry deposit: A case history for Mt. Milligan: Geophysics, **62**, 1419–1431, doi: 10.1190/1.1444246.

Oldenburg, D. W., R. Shehktman, R. A. Eso, C. G. Farquharson, P. Eaton, B. Anderson, and B. Bolin, 2004, Closing the gap between research and practice in EM data interpretation: 74th Annual International Meeting, SEG, Expanded Abstracts, 1179–1183.

Sosa, A., A. A. Velasco, L. Velazquez, M. Argaez, and R. Romero, 2013, Constrained optimization framework for joint inversion of geophysical data sets: Geophysical Journal International, **195**, 1745–1762, doi: 10.1093/gji/ggt326.

Teal, L., and A. Benavides, 2010, History and geologic overview of the Yanacocha mining district, Cajamarca, Peru: Economic Geology, **105**, 1173–1190, doi: 10.2113/econgeo.105.7.1173.

Vozoff, K., and D. L. B. Jupp, 1975, Joint inversion of geophysical data: Geophysical Journal of the Royal Astronomical Society, **42**, 977–991, doi: 10.1111/j.1365-246X.1975.tb06462.x.

Ward, S. H., and G. W. Hohmann, 1988, Electromagnetic theory for geophysical applications, *in* M. N. Nabighian, ed., Electromagnetic methods in applied geophysics: vol. 1, SEG, 131–311.

Zonge, K. L., and L. J. Hughes, 1991, Controlled source audio-frequency magnetotellurics, *in* M. N. Nabighian, ed., Electromagnetic methods in applied geophysics: vol. 2, SEG, 713–809.